Article

Fast-Training Deep Learning Algorithm for Multiplex Quantification of Mammalian Bioproduction Metabolites via Contactless Short-Wave Infrared Hyperspectral Sensing

Anjana Hevaganinge,[#] Callie M. Weber,[#] Anna Filatova,[#] Amy Musser, Anthony Neri, Jessica Conway, Yiding Yuan, Maurizio Cattaneo, Alisa Morss Clyne, and Yang Tao*

Read Online

ACCESS		Metrics & More		Article Recommendations

ABSTRACT: Within the biopharmaceutical sector, there exists the need for a contactless multiplex sensor, which can accurately detect metabolite levels in real time for precise feedback control of a bioreactor environment. Reported spectral sensors in the literature only work when fully submerged in the bioreactor and are subject to probe fouling due to a cell debris buildup. The use of a short-wave infrared (SWIR) hyperspectral (HS) camera allows for efficient, fully contactless collection of large spectral datasets for metabolite quantification. Here, we report the development of an interpretable deep learning system, a convolution metabolite regression (CMR) approach that detects glucose and lactate concentrations using label-free contactless HS images of cell-free spent media samples from Chinese hamster ovary (CHO) cell growth flasks. Using a dataset of <500 HS images, these CMR algorithms achieved a competitive test root-mean-square error (RMSE) performance of glucose quantification within 27 mg/dL and lactate quantification within 20 mg/dL. Conventional Raman spectroscopy probes report a validation performance of 26 and 18 mg/dL for glucose and lactate, respectively. The CMR system trains within 10 epochs and uses a convolution encoder with a sparse bottleneck regression layer to pick the best-performing filters learned by CMR. Each of these filters is combined with existing interpretable models to produce a metabolite sensing system that automatically removes spurious predictions. Collectively, this work will advance the safe and efficient adoption of contactless deep learning sensing systems for fine control of a variety of bioreactor environments.
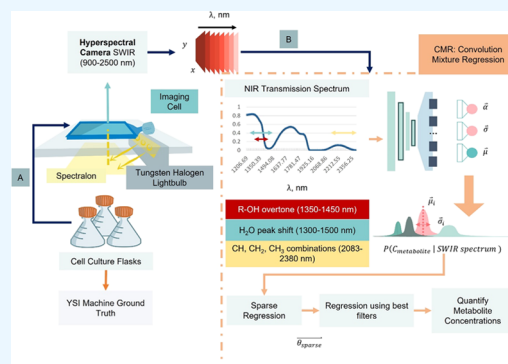
INTRODUCTION

A contactless sensor for measuring nutrients and metabolites is a valuable addition to the arsenal of process analytical tools available for producing high-quality cell-based therapeutic products. For example, the quality of post-translational modifications on monoclonal antibodies produced by Chinese hamster ovary (CHO) cells is affected by small changes in pH[2] or cell stress induced by sudden changes in glucose and lactate levels.[3] As such, pharmaceutical companies and researchers have dedicated significant resources toward the development of robust contactless sensors for fine bioprocess control.[4] Several iterations of spectroscopic sensors have been reported in the literature, with most recent papers focusing on the use of Raman fiber-optic probes.[5−10] These studies favor *in situ* Raman spectroscopy because of minimal interference from water in aqueous solutions while producing high-specificity "fingerprints" for different Raman-active molecules.[7] However, this fingerprint signal is weak and must compete with significant background autofluorescence from other biomolecules present in solution.[5] Because penetration depth of Raman probes is less than 12 μm,[11] probes must be fully submerged in

cell growth media. These probes are subject to increasing autofluorescence noise as cell density increases, explaining the sensor drift error seen in the literature.[12] In comparison, short-wave infrared (SWIR) spectroscopy achieves 0.5−5 mm[13] penetration depth while tolerating the presence of water with the analyte.[14] In fact, shifts in the water absorption band can be used as a molecular mirror that reflects the concentration of other solutes dissolved in the water hydrogen bond matrix.[15−18] This alleviates the need for both a submerged probe and sample processing prior to analysis. Both Raman and SWIR spectroscopy display highly nonlinear chemical vibrations that are difficult to simulate.[18] These weak, nonlinear signals are challenging to analyze and quantify
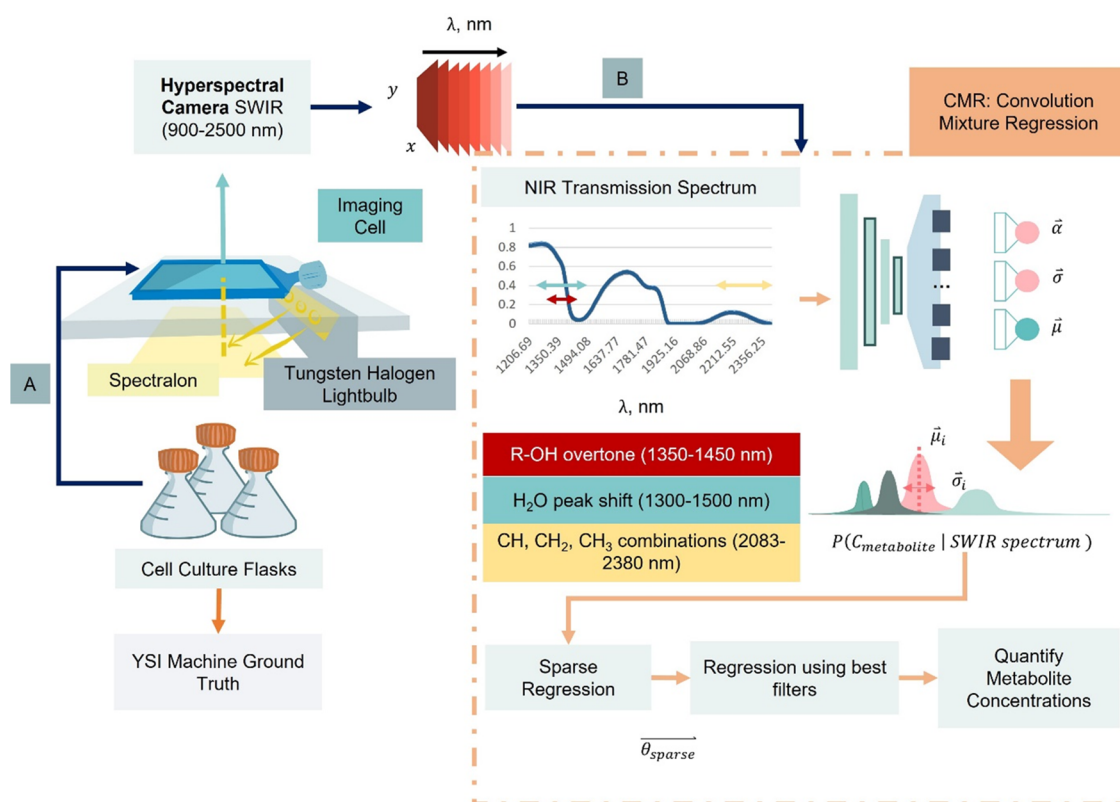
Figure 1. Overview of CMR network experimental design and architecture. (A) CHO cell dataset and ground truth metabolite readings are collected and used to train/evaluate (B) the interpretable CMR network.

without the use of chemometric machine learning models.[7,15,16,18] The use of fiber-optic probes limits dataset size to a few thousand samples, so only a handful of nonlinear chemometric analysis techniques have been applied to unravel these complex signals for metabolite regression. The most reported black-box chemometric technique has been partial least squares (PLS).[5−10,19] Such black-box models result in incomplete sensors that cannot self-diagnose spurious metabolite readings, making sensor troubleshooting and adaptation to low-cost settings difficult. SWIR hyperspectral imaging (HSI) is fully contactless and can record thousands of SWIR spectra in a single image.[20] This enables the efficient collection of large denoised spectral datasets by applying robust denoising techniques to each HS image.[21,22] Further, a single hyperspectral camera enables multiplex metabolite monitoring of multiple bioreactors in parallel, whereas multiple fiber-optic probes must be simultaneously calibrated for multivessel monitoring. Using this large dataset, deep interpretable models can be designed to highlight what parts of the input are omitted or how different features are combined by the model to generate final predictions.[23] These properties enable instantaneous troubleshooting of model predictions, or automatic filtering of drifting readouts. To enable efficient and high-quality biological production in bioreactors, there is a need to develop an accurate and interpretable contactless sensor that does not suffer from sensor drift.

The development of such a sensor must address three challenges. (1) Enable the efficient, cost effective collection of calibration data using a shaker flask cell growth system.[24] This labeled spectral dataset size must contain >10,000 samples, which enables the use of deep learning methods.[25,26] This interpretable deep learning model should (2) allow for

accurate metabolite quantification and (3) enable automatic detection and removal of unwanted metabolite measurements in real time. These three challenges form the objectives of this study. Each objective is met through the design of a SWIR HSI sensor with an interpretable convolutional metabolite regression (CMR) framework for rapid, contactless, and accurate quantification of glucose and lactate levels in Chinese hamster ovary (CHO) cell spent media (Figure 1).

The CMR algorithm uses a shallow deep convolutional encoder for feature extraction and sparse regression for metabolite quantification (Figure 1). It also features fast training, with competitive test performance generated within 10 epochs of training. Successful sensor implementation reduces both the need for highly trained specialists to obtain manual readings and the risk of breaking the sterility barrier. By enabling process automation, the contactless HSI sensor may also drive down labor costs while enabling the development of unique control strategies for continuous cell production.

■ EXPERIMENTAL SECTION

A large dataset of spent cell-free media hyperspectral images labeled with lactate and glucose concentrations is collected from eight CHO cell culture flasks. An automated preprocessing pipeline was designed to minimize noise caused by lighting variation, dust particles, and other artifacts in the hyperspectral image. The proposed system for glucose and lactate prediction from hyperspectral signals uses a deep convolution net encoder, followed by matrix inversion of the encoder latent space components for glucose, lactate, and cell viability prediction.[25] As shown in Figure 1, the latent space (bottleneck layer of a convolution net encoder) is first used

Table 1. Experimental Data Collection Time Points for Cell Culture Days 1−12

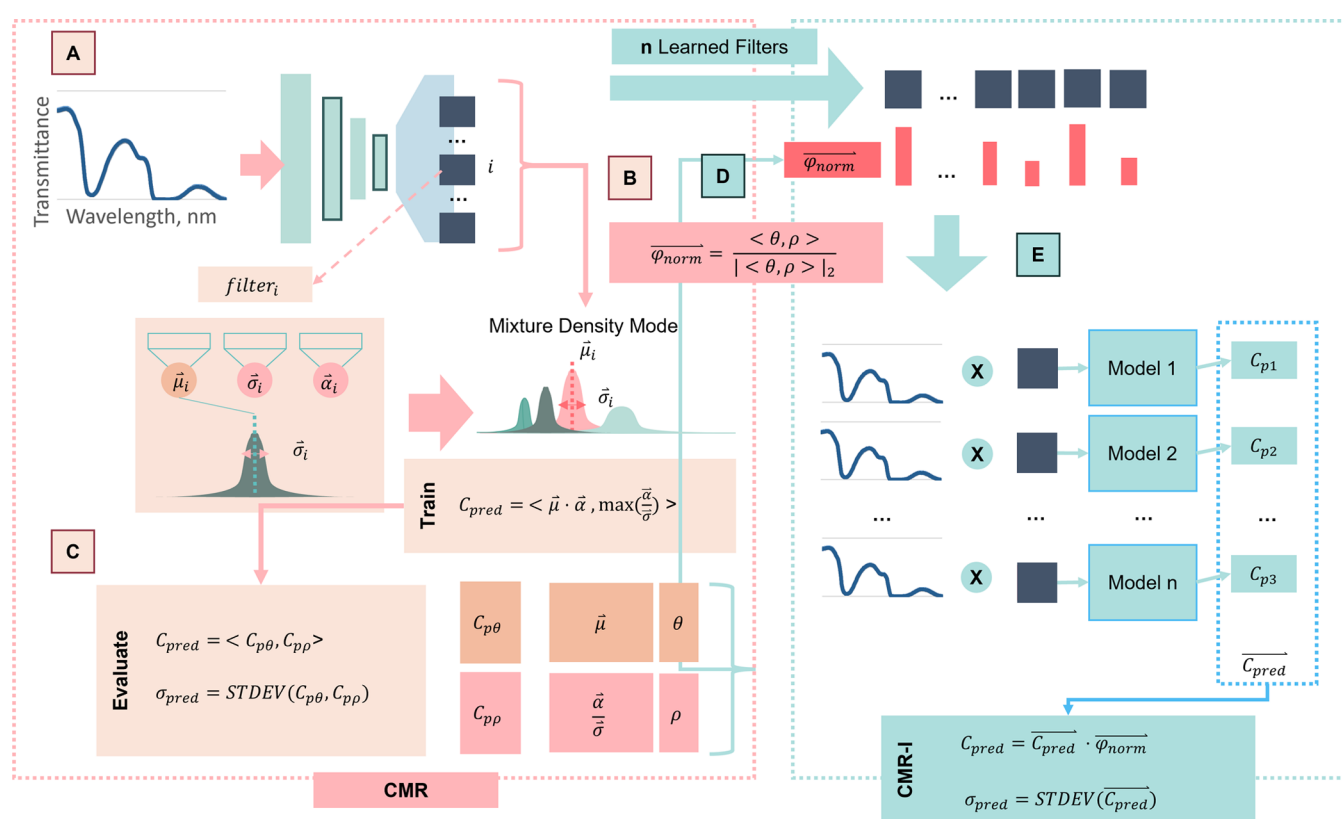| time	1	2	3	4	5	6	7	8	9	10	11	12
8:30 a.m.	x	x	x	x	x	x	x	x	x	x	x	x
11:00 a.m.			x	x	x	x	x	x				
2:30 p.m.			x	x	x	x	x	x				
4:30 p.m.		x	x	x	x	x	x	x	x	x	x	x
8:30 p.m.	x											

Figure 2. Architectural overview of CMR. (A, B) Each spectrum is first used to train the CMR network encoding layer; then (C) the bottleneck layer is used to select the best-performing encoder filters via sparse regression. (D, E) The trained filters and sparse weights are then used to train a suite of user-specified interpretable models for metabolite prediction.

to predict metabolite concentrations via sparse regression, and then these learned weights are used to pick the best learned convolution filters for use with parallel interpretable machine learning models like Gaussian process regression (GPR). Finally, the standard deviation of these predictions for each image was used to automatically filter out spurious metabolite predictions. CMR model performance was compared to partial least squares[27,28] models trained on polynomial features derived from the mean spectral signal of each HS image (Poly-PLS). Poly-PLS served as the baseline model for comparison with proposed CMR model variants.

CHO Cell Culture. Adalimumab-producing CHO cells (Creative Biolabs, Shirley, New York) were a generous gift from Artemis Biosystems, LLC (Quincy, Massachusetts). Cells were maintained in CD CHO Medium (Thermo Fisher Scientific) at 37 °C and 5% humidity and subcultured at a density of 3.0×10^5 cells/mL. To collect a varied range of samples, four cultures using 125 mL Erlenmeyer flasks (Corning Life Sciences) on a CO_2 resistant shaker (Thermo Fisher Scientific) set to 125 RPM were started at 8 a.m., and another four cultures after 12 h. The shaker was set to 135

RPM after 48 h. Cultures proceeded without passaging and were ended once all flasks reached a cell viability of 0%.

Experimental Data Collection. 630 μL media samples were collected from each cell culture flask at the times shown in Table 1. All samples were cultured for 12 days. Sample collection times were chosen to maximize data collection during the exponential growth phase of the cells (days 3−8). For each cell permeate sample, cuvettes were rinsed with 500 μL of 70% ethanol, dried with pressurized air, rinsed thrice with CD CHO Medium (Thermo Fisher Scientific), and dried with pressurized air. 500 μL of each centrifuged sample was loaded in a 1 mm quartz cuvette (Hellma USA Inc 110-1-40, Plainview, New York), taking care to avoid air bubbles and imaged three times using a 900−2500 nm SWIR hyperspectral sensor (Headwall Photonics, Bolton, Massachusetts).

Ground Truth Measurements. To quantify cell viability, 20 μL of each cell culture sample was combined with 20 μL of 0.4% trypan blue (Thermo Fisher Scientific) and counted with three technical replicates on a Countess II (Thermo Fisher Scientific). Total cell count, viable cell count, and percent viability were recorded. The remaining 610 μL of each cell sample was centrifuged at 8000*g* and 4 °C for 5 min to remove

cells. The supernatant was then removed and stored at 4 °C until use. Glucose and lactate concentrations were assessed using a YSI 2950 (Yellow Springs Instruments, 527690). All YSI metabolite measurements were normalized by division of 700 and 500 for glucose and lactate concentrations, respectively, prior to machine learning model training.

Building a Clean Dataset for Deep Metabolite Regression. To develop the deep learning prediction system, 600 hyperspectral images were acquired over 2 weeks of culturing CHO cells in cell culture flasks. First, the location of spent cell media in each hyperspectral image was masked out using the corresponding false RGB image. Next, all extracted pixels were randomly shuffled before a mean convolution was applied across all image pixels to reduce noise caused by lighting variations for each wavelength, producing the final dataset of clean spectral signals. Noise in the ground truth measurements of cell count, viability, glucose, and lactate was smoothed out using five sample Savitzky−Golay filtering.[21] In the literature, it is well known that deep neural networks can interpolate between training data points well but perform poorly when extrapolating beyond training data.[24] Therefore, the training dataset must contain a diverse array of samples that covers the usable data space. The data collected was naturally imbalanced, with a higher number of high-cell-viability images compared to low-cell-viability images. Data points with cell viability greater than 50% were used for model training. To minimize network extrapolation, data points with cell viability less than 80% were discarded during evaluation. Two flasks were reserved randomly from the remaining dataset for test data, and the rest of the data was used for training. Data from flasks 1 and 8 were used for validation of all models.

Data Analysis and Statistics. In this paper, three models were explored for contactless quantification of glucose and lactate using hyperspectral images of spent cell media. CMR is a fast-training deep learning model, the architecture of which is shown in Figure 2.

First, each spectrum is passed through the convolutional encoder into a compressed latent space (Figure 2A). Next, a mixture density model (MDN) of Gaussians is generated for each spectrum using mean, standard deviation, and α learned via each filter in the last convolution encoder layer (Figure 2B). During training, these mixture models were used to generate metabolite predictions. Equations 1−3 were used for training CMR net. During evaluation, sparse linear regression on these components was used to generate pixel-wise predictions of metabolite concentrations (Figure 2C). The highest weighted convolution encoder filters are then used to preprocess HSI pixel spectra for training several versions of any interpretable model of choice (Figure 2D), such as (Figure 2E) GPR in this case. Each prediction was weighed using the sparse weights from latent space sparse regression, and standard deviation of predicted metabolite concentrations from each GPR model was used for confidence interval calculations. CMR-I is an interpretable model which uses convolutional filters learned during CMR training for preprocessing spectra prior to training a series of interpretable ML models. In this case, Gaussian process regression models with Matern kernels were trained using the highest weighed convolution filters from the CMR convolution encoder. As a baseline approach, an average hyperspectral signal of each image was preprocessed using second-degree polynomial feature extraction prior to train PLS models with nine components (Poly-PLS).

CMR Architecture and Training. The CMR architecture (Figure 2A,B) was based on the mixture density model (MDN).[29] The CMR encoder consists of a series of one-dimensional (1D) convolutional filters with batch normalization and rectified linear unit activation. Each filter in the final layer of the CMR encoder is then used to estimate a single Gaussian with mean, variance, and weight α. All Gaussians in the latent space are then combined according to eq 1, where α is the learned weight of each Gaussian and μ is the mean, to generate the final training metabolite prediction. The number of filters in the final CMR encoder layer reflects the number of components in the CMR latent space ($n_{\text{latent space}}$), which was 30 in this case. Each filter was initialized using orthogonal weights to ensure that the learned filters form a sparse latent space for subsequent metabolite regression.[30] The CMR model was designed to transform highly redundant SWIR spectra to a compact latent space, which clearly separates varying metabolite concentrations while automatically identifying spurious spectra, which are difficult to quantify and lead to sudden sensor errors. In particular, a β-variational autoencoder architecture was modified to transform these spectral signals into a compressed latent space that smoothly distinguishes different metabolite concentrations.[25,31] The losses used to train CMR reflect these criteria (eq 2). The CMR loss consists of L1 loss between ground truth metabolite concentration (C_{True}) and concentration predicted by eq 1 (C_{Pred}) and evidence lower bound (ELBO) loss. The ELBO loss is composed of the KL-divergence (D_{KL}) between a Gaussian multivariate distribution $\mathcal{N}(\vec{\mu}, \vec{\sigma})$ specified by the CMR latent space and a Gaussian distribution $\mathcal{N}(0, 1)$ with mean 0 and unit variance and the likelihood (LL) of C_{True} in Gaussian multivariate distribution $\mathcal{N}(\vec{\mu}, \vec{\sigma})$ specified by the CMR latent space (eq 3). L1 loss and LL loss ensured that the learned latent space could distinguish different metabolite concentrations with high accuracy, while D_{KL} loss ensured that the learned latent space varies smoothly with spectral differences, allowing for smooth interpolation of unknown metabolite concentrations. CMR training was conducted using randomly sampled batches of hyperspectral pixel spectra sampled across all training images (batch size 5000 spectra). All models were only trained for 10 epochs. Because the training process is so fast, 16 different cross-validation folds for each metabolite were trained within a few hours, for a total of 32 trained CMR models.

$$C_{\text{pred}} = 0.5 \times \left(\vec{\mu} \cdot \vec{\alpha} + \max\left(\frac{\vec{\alpha}}{\vec{\sigma}} \right) \right) \tag{1}$$

$$\text{CMR loss} = \sum |C_{\text{True}} - C_{\text{Pred}}| + \text{ELBO} \tag{2}$$

$$\text{ELBO} = \beta \times D_{\text{KL}}(\mathcal{N}(\vec{\mu}, \vec{\sigma}) \| \mathcal{N}(0, 1)) - \text{LL}(C_{\text{True}}, \mathcal{N}(\vec{\mu}, \vec{\sigma})) \tag{3}$$

CMR Evaluation. During CMR model evaluation, the latent spaces $\vec{\mu}$, $\vec{\sigma}$, and $\vec{\alpha}$ were combined and used as features in a sparse linear regression model for metabolite regression (Figure 2C). Latent space regression models are formed using $\vec{\mu}$ and $\frac{\vec{\alpha}}{\vec{\sigma}}$, which are considered output estimates of a traditional MDN model.[29] Weights θ and ρ were learned, respectively, for $\vec{\mu}$ and $\frac{\vec{\alpha}}{\vec{\sigma}}$ via matrix inversion.[25] Weights were then clipped by 2× minimum regression weight,

Table 2. Statistical Comparison of Contactless Glucose Quantification with Cell Culture Flask Datasets

	train				valid				test			
	MAE	MAPE	RMSE	r^2	MAE	MAPE	RMSE	r^2	MAE	MAPE	RMSE	r^2
CMR[a]	19.40	0.16	26.07	0.97	30.98	0.23	44.16	0.91	21.45	0.17	27.63	0.97
CMR-I[a]	17.80	0.15	22.07	0.97	29.14	0.20	41.41	0.92	22.11	0.16	27.04	0.95
poly-PLS	22.06	0.20	30.41	0.96	28.41	0.25	43.71	0.92	23.69	0.19	30.05	0.96

[a]Indicates deep learning models.

Table 3. Statistical Comparison of Contactless Lactate Quantification with Cell Culture Flask Datasets

	train				valid				test			
	MAE	MAPE	RMSE	r^2	MAE	MAPE	RMSE	r^2	MAE	MAPE	RMSE	r^2
CMR[a]	14.06	0.08	22.25	0.92	15.25	0.11	19.75	0.95	14.88	0.10	19.19	0.94
CMR-I[a]	11.97	0.07	16.45	0.92	13.39	0.07	18.61	0.95	15.51	0.10	19.39	0.91
poly-PLS	15.41	0.09	22.86	0.91	13.12	0.08	18.17	0.95	15.36	0.09	19.22	0.93

[a]Indicates deep learning models.

and remaining features are used to create a sparse linear regression via matrix inversion. The mean metabolite prediction for each image was reported as the final predicted metabolite concentration (eq 4). $C_{p\theta}$ is the concentration predicted using sparse regression of $\vec{\mu}$, and $C_{p\rho}$ is the concentration predicted using sparse regression of $\frac{\vec{\alpha}}{\vec{\sigma}}$. The standard deviation between the predicted metabolite concentration from $\vec{\mu}$ and $\frac{\vec{\alpha}}{\vec{\sigma}}$ models was used for automated filtering of noisy metabolite predictions (eq 5). It was assumed that the deviation between these predictions reflects the uncertainty of the model in each metabolite prediction.

$$C_{pred} = \langle C_{p\theta}, C_{p\rho} \rangle \tag{4}$$

$$\sigma_{pred} = STDEV(C_{p\theta}, C_{p\rho}) \tag{5}$$

CMR-I Evaluation and Filtering. After training, CMR learned several useful filters. The information compression efficiency of each filter is reflected by the strength of sparse weights θ and ρ assigned to each latent space component. First, the mean spectra from each HSI image were convolved with each learned filter prior to fitting an interpretable model to each respective convolution filter processed spectra, as shown in Figure 2D,E. $\overrightarrow{C_{pred}}$ represents the vector of metabolite predictions generated by this set of models. In this paper, a Gaussian process regression model was used with Matern kernel (length scale = 10, nu = 2.5) with a fixed length scale.[27] The average normalized regression weight (φ_{norm}, eq 6) was used to weight the metabolite predictions of each interpretable model and generate the final metabolite prediction (eq 7). It was assumed that the deviation between these predictions (eq 8) reflects the uncertainty of the model in each metabolite prediction. All predictions with normalized predicted standard deviation greater than 0.03 were then discarded to produce filtered metabolite predictions.

$$\varphi_{norm} = \frac{\langle \theta, \rho \rangle}{|\langle \theta, \rho \rangle|_2} \tag{6}$$

$$C_{pred} = \overrightarrow{C_{pred}} \times \overrightarrow{\varphi_{norm}} \tag{7}$$

$$\sigma_{pred} = STDEV(\overrightarrow{C_{pred}}) \tag{8}$$

RESULTS

Training an accurate AI model requires a large, comprehensive dataset with accurate labels. Traditional spectroscopy instruments are unable to provide sufficiently large datasets in an efficient manner, but the HSI camera can collect thousands of sample signals within a single image. Consequently, a high-quality dataset was collected in-house using labeled HSI images of spent cell media sampled from eight CHO cell culture flasks. This dataset was then divided into 16 cross-validation folds for robust analysis of model performance. For each fold, data from six flasks was used for training, and two flasks were randomly sampled for use as test data. This split was considered the most robust train−test split for assessing model performance generalizability.

Performance of Deep Metabolite Regression Compared to Gold Standard Measurement. To evaluate model performance, cross-validation fold methods were applied to the initial training/validation dataset collected using shaker flask experiments. Table 2 summarizes average glucose quantification performance across 16 cross-validation folds for CMR, CMR-I, and Poly-PLS. Poly-PLS was presented as a baseline black-box model to compare against all variants of CMR. Each cross-validation fold consisted of six training cell culture flasks and two test flasks. Cell culture flasks 1 and 8 were reserved as validation flasks. Across all folds, CMR-I achieves the lowest mean absolute error (MAE), mean absolute percentage error (MAPE), root-mean-square error (RMSE). The r^2 values are quite similar across all models. Table 3 summarizes average lactate quantification performance for CMR, CMR-I, and Poly-PLS. All three models demonstrate very similar performance across all datasets, but CMR displays the best MAE, RMSE, and r^2 for lactate prediction among the test folds.

CMR-I Interpretability and Performance Evaluation. Although model interpretability has not been standardized in the literature to date, it is possible to define a qualitative set of criteria within a specific domain that classify a machine learning model as "interpretable".[32] In the biopharmaceutical domain, an interpretable model should (1) map highly redundant spectra to a compressed space that easily separates spectra based on metabolite concentration, (2) generate confidence intervals for each metabolite prediction, and (3) adapt easily to varying bioreactor environments and new metabolites. Generated confidence intervals can then be used to automatically detect and remove spurious metabolite
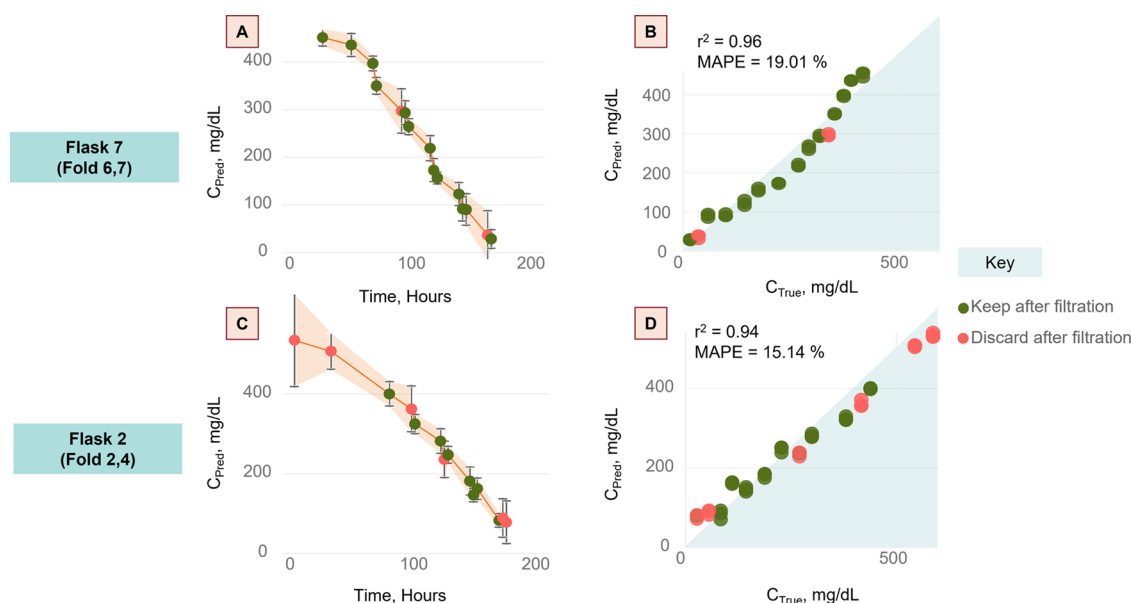
Figure 3. Glucose test trajectories generated by CMR-I after filtering for (A) flask 7 (cross-validation fold (6,7)) and (C) flask 2 (cross-validation fold (2,4)). Correlation visualization between ground truth (C_{true}) glucose concentration and concentration predicted by CMR-I (C_{pred}) are shown with r^2 and MAPE % values for each cross-validation fold listed in the top left corner for (B) flask 7 and (D) flask 2. Green points are kept after filtration, and red points are discarded after automatic filtration.
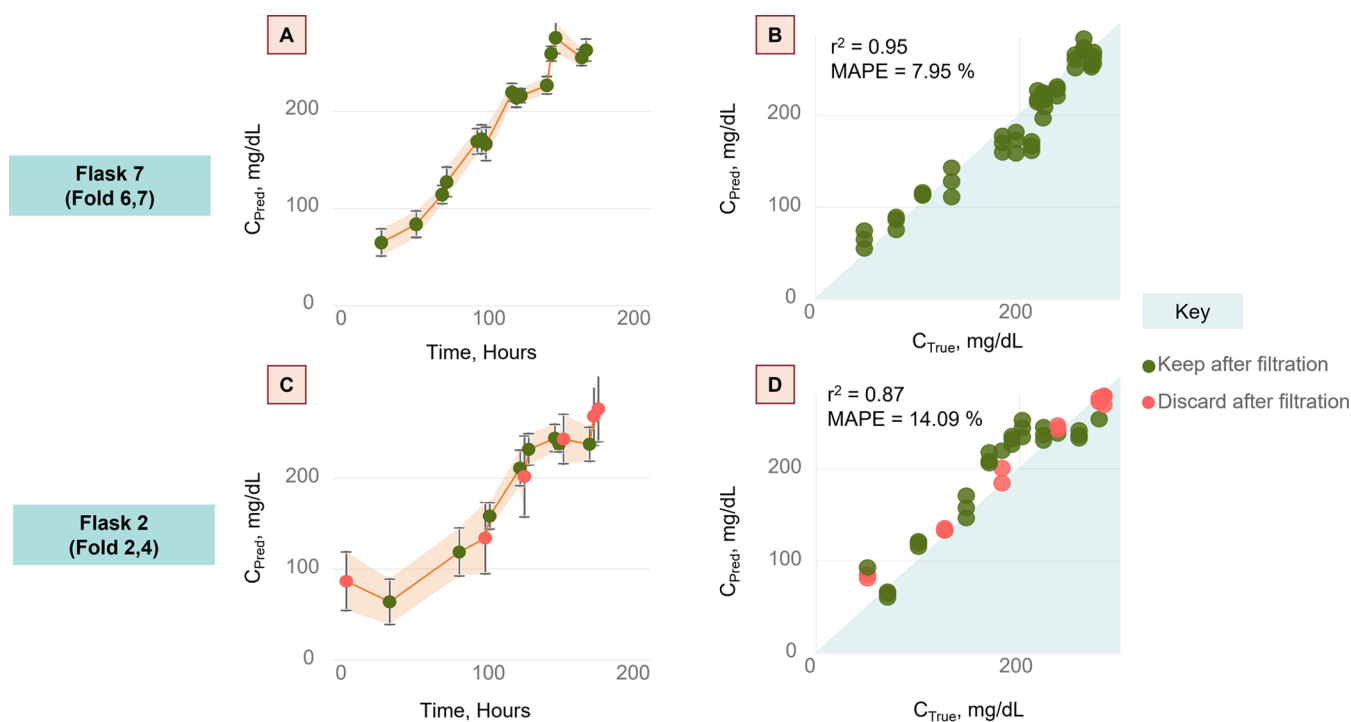

Figure 4. Lactate test trajectories generated by CMR-I after filtering for (A) flask 7 (cross-validation fold (6,7)) and (C) flask 2 (cross-validation fold (2,4)). Correlation visualization between ground truth (C_{true}) lactate concentration and concentration predicted by CMR-I (C_{pred}) are shown with r^2 and MAPE % values for each cross-validation fold listed in the top left corner for (B) flask 7 and (D) flask 2. Green points are kept after filtration, and red points are discarded after automatic filtration.

predictions. CMR-I was developed as a fully interpretable model with automated filtering of spurious metabolite predictions. Visualization of metabolite trajectories generated by CMR-I after filtering for two sample test folds are shown for glucose (Figure 3A,C) and lactate (Figure 4A,C), respectively, with 95% confidence intervals indicated by error bars and light shading. Visualization of model correlation to ground truth metabolite measurement is shown for glucose (Figure 3B,D)

and lactate (Figure 4B,D) using two sample test folds. r^2 and MAPE after filtering are listed for each fold in the top left corner of each graph. Red points are automatically removed via CMR-I filtering, while green points are kept.

Because CMR net trains within 10 epochs (Figure 5), 16 different cross-validation folds for each metabolite were trained within a few hours.
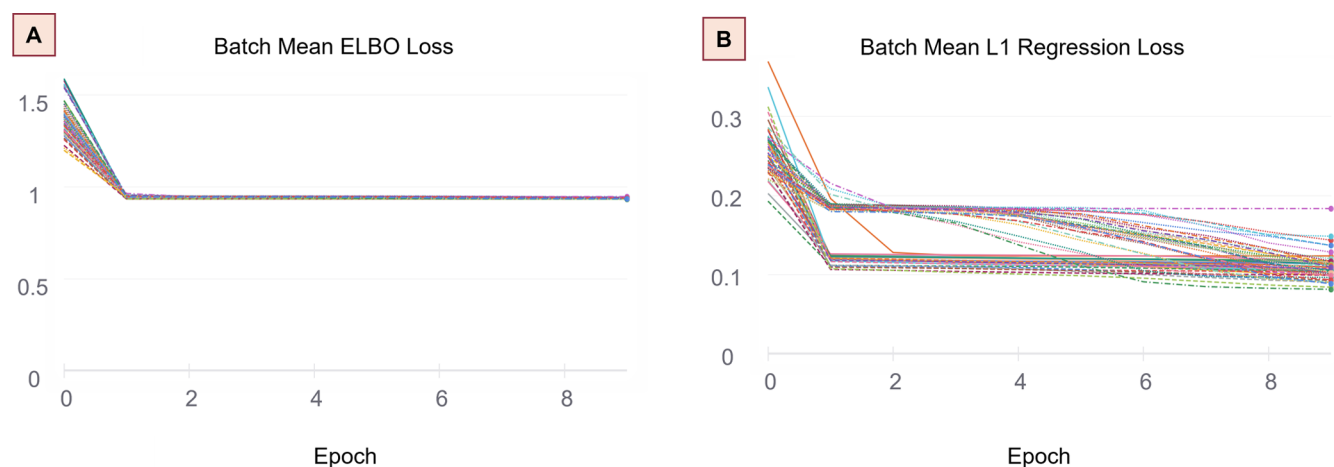
Figure 5. Training history curves for (A) ELBO loss and (B) mean L1 loss across all metabolites and folds for CMR deep learning network. All results presented in this paper use CMR models that were trained for only 10 epochs.
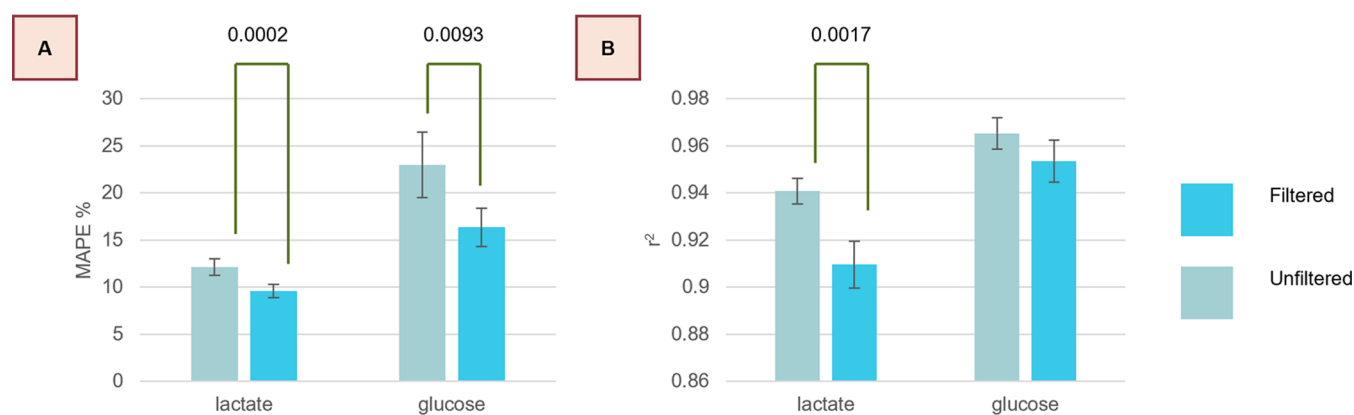

Figure 6. Test dataset statistical performance comparison of CMR-I for contactless measurement of glucose and lactate before (unfiltered) and after (filtered) automated filtering. Average (A) MAPE % and (B) r^2 are shown across all cross-validation test datasets; p values are listed above each significant difference as determined by two-sided Wilcoxon rank-sum test. The error bars represent the standard error across all cross-validation folds.

Model performance across these folds was then used to assess if prediction improvements caused by automated CMR filtering are statistically significant. Prior to calculation of evaluation metrics, all normalized metabolite concentrations less than 0.01 were removed to avoid unstable MAPE calculations. Comparison of metabolite prediction performance across all test data folds by the interpretable CMR-I model before and after filtering are shown in Figure 6. CMR filtering significantly improved average MAPE by 21 and 29% for lactate and glucose, respectively, but significantly reduces average r^2 by 3% for lactate.

■ DISCUSSION

This study combined several methods across diverging disciplines to achieve a truly contactless sensor for bioreactor cell cultivation. The method achieved average r^2 values of more than 0.9 on test datasets. The study design included samples taken from a variety of cell culture flasks that were cultured and sampled at different time points, which highlights the robustness of the proposed method. The use of a hyperspectral camera for contactless deep learning detection of key metabolites in cell culture perfusate has not been attempted by previous work to our knowledge. Instead, prior works have attempted to monitor glucose, lactate, and other key metabolites using invasive NIR fiber-optic probes[9,19] and Raman spectroscopy probes,[5−9] among others.[10] However, these probes were highly sensitive to noise caused by lighting variations and exhibited measurement drift. Because it is difficult to efficiently collect large datasets using probes, these studies are limited to small dataset chemometric techniques like PLS. While Raman spectroscopy has demonstrated accurate glucose prediction to within 26 mg/dL, it has limited resolution for other metabolites, as evidenced by the variable reported accuracy for other metabolites. For example, Matthews et al. only report lactate prediction accuracies up to 116 mg/dL.[5] Other sources report Raman spectroscopy probe validation performance of 26 and 18 mg/dL for glucose and lactate, respectively, in the literature.[1] The literature review revealed several sources that use deep learning analysis of hyperspectral reflectance images in the food industry for automated produce processing,[33] but no sources have attempted to bring these techniques to the biopharmaceutical arena. This study boasts test RMSE prediction accuracy within 27 mg/dL for glucose using the CMR-I model and 19.2 mg/dL for lactate. To the best of our knowledge, no previous studies have reported the automatic filtering of spurious metabolite predictions. The CMR-I model can significantly improve metabolite prediction performance (Figure 6) using a relatively
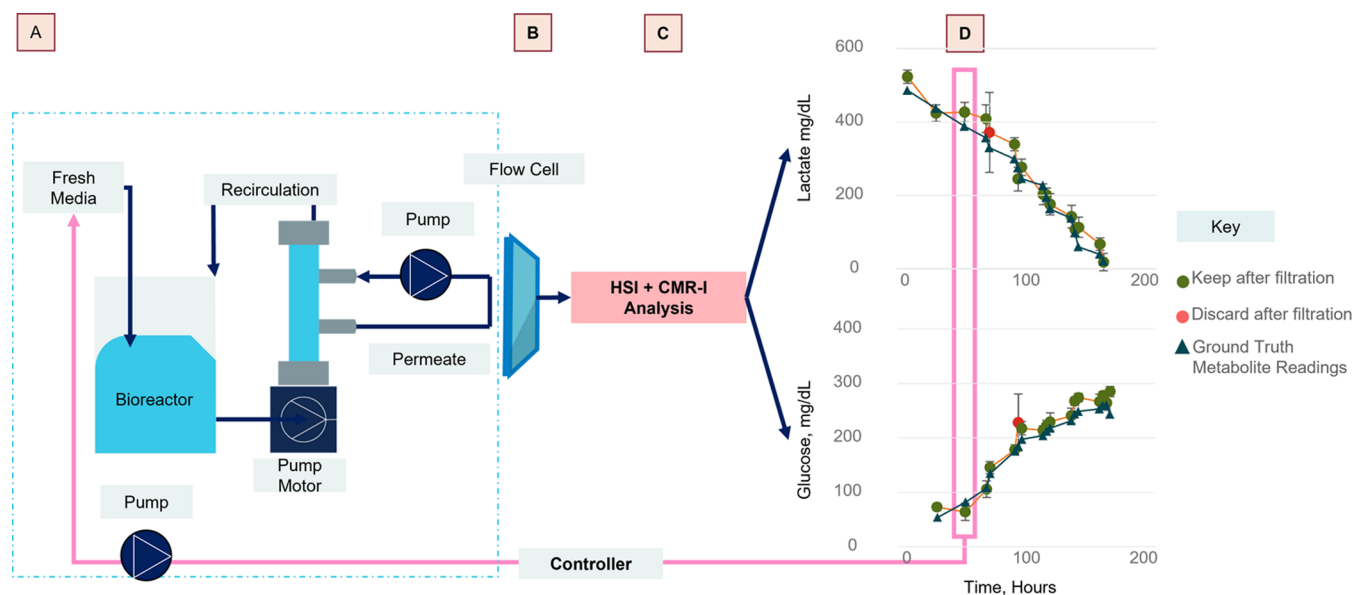
Figure 7. Future Application of the HSI + CMR sensor for real-time monitoring and control of bioreactor environment. (A) Permeate from the bioreactor system flows through (B) a quartz flow cell and then is imaged and analyzed by (C) the HSI + CMR analysis system to produce (D) contactless metabolite trajectories in real time with automatic filtering of spurious metabolite predictions. These predictions can then be used to finely control the addition of cell media to the bioreactor.

simple filtering technique afforded by the interpretable architecture of CMR-I algorithm. Through comparison of average lactate prediction performance before and after CMR-I filtering (Figure 6), the r^2 value is reduced by 3% but the MAPE is improved by 21%. This suggests that the CMR-I filter effectively removed spurious predictions but artificially lowered r^2 through removal of extreme lactate concentrations.

This study takes advantage of the large spectral dataset acquired using hyperspectral images to train shallow, interpretable deep learning models that exhibit fast training times and high prediction accuracies within an interpretable framework that allows for model robustness analysis and troubleshooting. This large dataset is also used to train a modified polynomial PLS model using the median spectral signal of each image. Most works in the literature attempt to explain deep network predictions using different versions of attention maps.[23,26] These methods are sufficient for identification of regions of interest used for network predictions. However, they do not illuminate what parts of the input are omitted or how different pieces of information are combined.[23] First, the sparse regression of the CMR bottleneck layer was easy to interpret based on the sparse weights learned for each metabolite. These weights clearly showed which corresponding hidden node filters are most influential for resulting metabolite prediction. These learned filters were then used to preprocess the hyperspectral signals prior to training an interpretable model like GPR in this case.

The hyperspectral camera acts as a multiplex metabolite sensor that is only limited in metabolite sensitivity by the training dataset. After all, SWIR spectroscopy can be used to monitor any metabolite that disturbs the hydrogen bonding network of water molecules in aqueous solution.[15−18] These signals are both noisy and redundant; very different metabolite concentrations can produce nearly identical spectral signals. Therefore, a simple thresholding filter based on the standard deviation of CMR-I model predictions from each learned filter was used to remove spurious metabolite predictions. As shown

in Figure 6, this filter significantly improved metabolite prediction performance, and effectively removed noisy outlier predictions in real time to produce a smooth noncontactless metabolite trajectory that can be easily incorporated into traditional feedback control algorithms for precise control of bioreactor environments (Figure 7). Only a robust cell filtration device is required to collect permeate from the bioreactor vessel (Figure 7A) for HS imaging and analysis. In this paper, all training, validation, and test datasets were collected within the same timeframe.

Our study balanced prediction accuracy with model depth and dataset size to create a SWIR hyperspectral contactless sensor framework for various cell metabolites. Rather than increasing the CMR encoder complexity for better performance, efforts were directed at automatically cleaning hyperspectral images to remove any errant signals caused by image lighting variations, dust, etc. Further, the network architecture was optimized to perform well with spectral signals that look nearly identical and are only separable by subtle correlated shifts. The ability of an autoencoder to generate many types of useful coordinate transforms is directed toward metabolite separability though the use of sparse singular-value decomposition (SVD) regression during evaluation rather than training.[25] Within this space, sparse polynomial regression was applied to generate parsimonious and interpretable models for any metabolite of choice.

Limitations of our study include that all images are taken of cell-free perfusate, rather than bioreactor cell culture, to minimize light scattering caused by the presence of cells. In other words, cell growth media must be filtered of cells prior to imaging. Future studies should explore the use of CMR for analysis of unfiltered cell culture media. Further, all cell permeate samples were extracted from 125 mL cell culture flasks for training, validation, and test datasets. Metabolite mixing in larger vessels may not be as uniform as in smaller vessels, so the permeate may not reflect the bioreactor environment.[10] In industry, bioreactor vessels are as large as

10,000 L, so the CMR framework should be tested using these larger vessels. Finally, metabolite regression accuracy can be improved though the use of high-performance liquid chromatography (HPLC) to collect ground truth metabolite readings rather than the YSI machine. This also expands the range of metabolites that can be trained for accurate quantification using the CMR-HSI contactless sensor framework.

CONCLUSIONS

This study reports the development of a SWIR HS sensor with interpretable deep learning metabolite regression, which addresses the three challenges preventing widespread adoption of real-time bioprocess monitoring. The reported SWIR HS sensor framework (1) enables efficient contactless collection of calibration data using a shaker flask cell growth system within 2 weeks.[24] This labeled spectral dataset contains millions of spectral samples, which enables the use of deep learning methods.[25,26] The interpretable CMR-I model (2) boasts competitive metabolite quantification performance with quick training time of 10 epochs and (3) enables automatic detection and removal of unwanted metabolite measurements in real time. Currently, HPLC and YSI machines remain the gold standard for bioprocess monitoring. These sensors cannot monitor metabolites in real time since they require invasive sample collection for subsequent sample preparation and analysis at a remote lab. Experimental real-time sensors consist of *in situ* probes that are subject to probe fouling over time by cells in the bioreactor. Our system demonstrates a robust contactless multiplex sensor for metabolite monitoring during bioreactor cell cultivation. The interpretable nature of this system may stimulate faster adoption of this sensor within a high-stakes bioprocess environment.

AUTHOR INFORMATION

Corresponding Author

Yang Tao − *Fischell Department of Bioengineering, University of Maryland, College Park, Maryland 20742, United States*; Email: ytao@umd.edu

Authors

Anjana Hevaganinge − *Fischell Department of Bioengineering, University of Maryland, College Park, Maryland 20742, United States;* ⬤ orcid.org/0000-0002-6787-4322

Callie M. Weber − *Fischell Department of Bioengineering, University of Maryland, College Park, Maryland 20742, United States;* ⬤ orcid.org/0000-0001-6324-3657

Anna Filatova − *Fischell Department of Bioengineering, University of Maryland, College Park, Maryland 20742, United States*

Amy Musser − *Fischell Department of Bioengineering, University of Maryland, College Park, Maryland 20742, United States*

Anthony Neri − *Fischell Department of Bioengineering, University of Maryland, College Park, Maryland 20742, United States*

Jessica Conway − *Fischell Department of Bioengineering, University of Maryland, College Park, Maryland 20742, United States*

Yiding Yuan − *Fischell Department of Bioengineering, University of Maryland, College Park, Maryland 20742, United States*

Maurizio Cattaneo − *Fischell Department of Bioengineering, University of Maryland, College Park, Maryland 20742, United States; Artemis Biosystems, Woburn, Massachusetts 02169, United States*

Alisa Morss Clyne − *Fischell Department of Bioengineering, University of Maryland, College Park, Maryland 20742, United States*

Complete contact information is available at:
https://pubs.acs.org/10.1021/acsomega.3c00861

Author Contributions

#A.H., C.M.W., and A.F. are co-first authors.

Notes

The authors declare no competing financial interest.

REFERENCES

(1) Rafferty, C.; Johnson, K.; O'Mahony, J.; Burgoyne, B.; Rea, R.; Balss, K. M. Analysis of Chemometric Models Applied to Raman Spectroscopy for Monitoring Key Metabolites of Cell Culture. *Biotechnol. Prog.* **2020**, *36*, No. e2977.

(2) Joshi, V.; Shivach, T.; Kumar, V.; Yadav, N.; Rathore, A. Avoiding Antibody Aggregation during Processing: Establishing Hold Times. *Biotechnol. J.* **2014**, *9*, 1195−1205.

(3) Pereira, S.; Kildegaard, H. F.; Andersen, M. R. Impact of CHO Metabolism on Cell Growth and Protein Production: An Overview of Toxic and Inhibiting Metabolites and Nutrients. *Biotechnol. J.* **2018**, *13*, No. 1700499.

(4) Claßen, J.; Aupert, F.; Reardon, K. F.; Solle, D.; Scheper, T. Spectroscopic Sensors for In-Line Bioprocess Monitoring in Research and Pharmaceutical Industrial Application. *Anal. Bioanal. Chem.* **2017**, *409*, 651−666.

(5) Matthews, T. E.; Smelko, J. P.; Berry, B.; Romero-Torres, S.; Hill, D.; Kshirsagar, R.; Wiltberger, K. Glucose Monitoring and Adaptive Feeding of Mammalian Cell Culture in the Presence of Strong Autofluorescence by near Infrared Raman Spectroscopy. *Biotechnol. Prog.* **2018**, *34*, 1574−1580.

(6) Whelan, J.; Craven, S.; Glennon, B. In Situ Raman Spectroscopy for Simultaneous Monitoring of Multiple Process Parameters in Mammalian Cell Culture Bioreactors. *Biotechnol. Prog.* **2012**, *28*, 1355−1362.

(7) Esmonde-White, K. A.; Cuellar, M.; Lewis, I. R. The Role of Raman Spectroscopy in Biopharmaceuticals from Development to Manufacturing. *Anal. Bioanal. Chem.* **2022**, *414*, 969−991.

(8) Rafferty, C.; O'Mahony, J.; Rea, R.; Burgoyne, B.; Balss, K. M.; Lyngberg, O.; O'Mahony-Hartnett, C.; Hill, D.; Schaefer, E. Raman Spectroscopic Based Chemometric Models to Support a Dynamic Capacitance Based Cell Culture Feeding Strategy. *Bioprocess Biosyst. Eng.* **2020**, *43*, 1415−1429.

(9) Kozma, B.; Hirsch, E.; Gergely, S.; Párta, L.; Pataki, H.; Salgó, A. On-Line Prediction of the Glucose Concentration of CHO Cell Cultivations by NIR and Raman Spectroscopy: Comparative Scalability Test with a Shake Flask Model System. *J. Pharm. Biomed. Anal.* **2017**, *145*, 346−355.

(10) Claßen, J.; Aupert, F.; Reardon, K. F.; Solle, D.; Scheper, T. Spectroscopic Sensors for In-Line Bioprocess Monitoring in Research and Pharmaceutical Industrial Application. *Anal. Bioanal. Chem.* **2016**, *409*, 651−666.

(11) Adar, F.; Lee, E.; Mamedov, S.; Whitley, A. Experimental Evaluation of the Depth Resolution of a Raman Microscope. *Microsc. Microanal.* **2010**, *16*, 360−361.

(12) Hu, J.; Chen, G.; Yongjun, Q. I. N.; Zhou, W. A Raman Spectroscopy Integrated Perfusion Cell Culture System for Monitoring and Auto-Controlling Perfusion Cell Culture. WO2020238918A1, 2020.

(13) Padalkar, M. V.; Pleshko, N. Wavelength-Dependent Penetration Depth of near Infrared Radiation into Cartilage. *Analyst* **2015**, *140*, 2093−2100.

(14) Katiyi, A.; Karabchevsky, A. Si Nanostrip Optical Waveguide for On-Chip Broadband Molecular Overtone Spectroscopy in near-Infrared. *ACS Sens.* **2018**, *3*, 618−623.

(15) Tsenkova, R.; Munćan, J.; Pollner, B.; Kovacs, Z. Essentials of Aquaphotomics and Its Chemometrics Approaches. *Front. Chem.* **2018**, *6*, No. 363.

(16) Czarnecki, M. A.; Morisawa, Y.; Futami, Y.; Ozaki, Y. Advances in Molecular Structure and Interaction Studies Using Near-Infrared Spectroscopy. *Chem. Rev.* **2015**, *115*, 9707−9744.

(17) Kojić, D.; Tsenkova, R.; Tomobe, K.; Yasuoka, K.; Yasui, M. Water Confined in the Local Field of Ions. *ChemPhysChem* **2014**, *15*, 4077−4086.

(18) Beć, K. B.; Grabska, J.; Huck, C. W.; Ozaki, Y. Quantum Mechanical Simulation of Near-Infrared Spectra: Applications in Physical and Analytical Chemistry. *Mol. Spectrosc. Quantum Chem. Approach* **2019**, *2*, 353−388.

(19) Chen, J.; Arnold, M. A.; Small, G. W. Comparison of Combination and First Overtone Spectral Regions for Near-Infrared Calibration Models for Glucose and Other Biomolecules in Aqueous Solutions. *Anal. Chem.* **2004**, *76*, 5405−5413.

(20) Mouroulis, P.; Green, R. O. Review of High Fidelity Imaging Spectrometer Design for Remote Sensing. *Opt. Eng.* **2018**, *57*, No. 040901.

(21) Rinnan, Å.; Van Den Berg, F.; Engelsen, S. B. Review of the Most Common Pre-Processing Techniques for near-Infrared Spectra. *TrAC, Trends Anal. Chem.* **2009**, *28*, 1201−1222.

(22) Kojić, D.; Tsenkova, R.; Yasui, M. Improving Accuracy and Reproducibility of Vibrational Spectra for Diluted Solutions. *Anal. Chim. Acta* **2017**, *955*, 86−97.

(23) Rudin, C. Stop Explaining Black Box Machine Learning Models for High Stakes Decisions and Use Interpretable Models Instead. *Nat. Mach. Intell.* **2019**, *1*, 206−215.

(24) Karniadakis, G. E.; Kevrekidis, I. G.; Lu, L.; Perdikaris, P.; Wang, S.; Yang, L. Physics-Informed Machine Learning. *Nat. Rev. Phys.* **2021**, *3*, 422−440.

(25) Champion, K.; Lusch, B.; Kutz, J. N.; Brunton, S. L. Data-Driven Discovery of Coordinates and Governing Equations. *Proc. Natl. Acad. Sci. U.S.A.* **2019**, *116*, 22445−22451.

(26) Zhang, Y.; Tiňo, P.; Leonardis, A.; Tang, K. A Survey on Neural Network Interpretability. *IEEE Trans. Emerg. Top. Comput. Intell.* **2021**, *5*, 726−742.

(27) Pedregosa, F.; Varoquaux, G.; Gramfort, A.; Michel, V.; Thirion, B.; Grisel, O.; Blondel, M.; Prettenhofer, P.; Weiss, R.; Dubourg, V.; Vanderplas, J.; Passos, A.; Cournapeau, D.; Brucher, M.; Perrot, M.; Duchesnay, E. Scikit-Learn: Machine Learning in {P}ython. *J. Mach. Learn. Res.* **2011**, *12*, 2825−2830.

(28) Abdi, H. Partial Least Squares Regression and Projection on Latent Structure Regression (PLS Regression). *Wiley Interdiscip. Rev.: Comput. Stat.* **2010**, *2*, 97−106.

(29) Bishop, C. M. *Mixture Density Networks*, Technical Report; Aston University: Birmingham, 1994.

(30) Saxe, A. M.; McClelland, J. L.; Ganguli, S. Exact Solutions to the Nonlinear Dynamics of Learning in Deep Linear Neural Networks, arXiv:1312.6120. arXiv.org e-Print archive, 2013. https://doi.org/10.48550/arXiv.1312.6120.

(31) Higgins, I.; Matthey, L.; Pal, A.; Burgess, C.; Glorot, X.; Botvinick, M.; Mohamed, S.; Lerchner, A. In *Beta-Vae: Learning Basic Visual Concepts with a Constrained Variational Framework*, International Conference on Learning Representations, 2016.

(32) Rudin, C. Stop Explaining Black Box Machine Learning Models for High Stakes Decisions and Use Interpretable Models Instead. *Nat. Mach. Intell.* **2019**, *1*, 206−215.

(33) Liu, Y.; Pu, H.; Sun, D. W. Hyperspectral Imaging Technique for Evaluating Food Quality and Safety during Various Processes: A Review of Recent Applications. *Trends Food Sci. Technol.* **2017**, *69*, 25−35.